PCCP

Physical Chemistry Chemical Physics

rsc.li/pccp

25 YEARS ANNIVERSARY
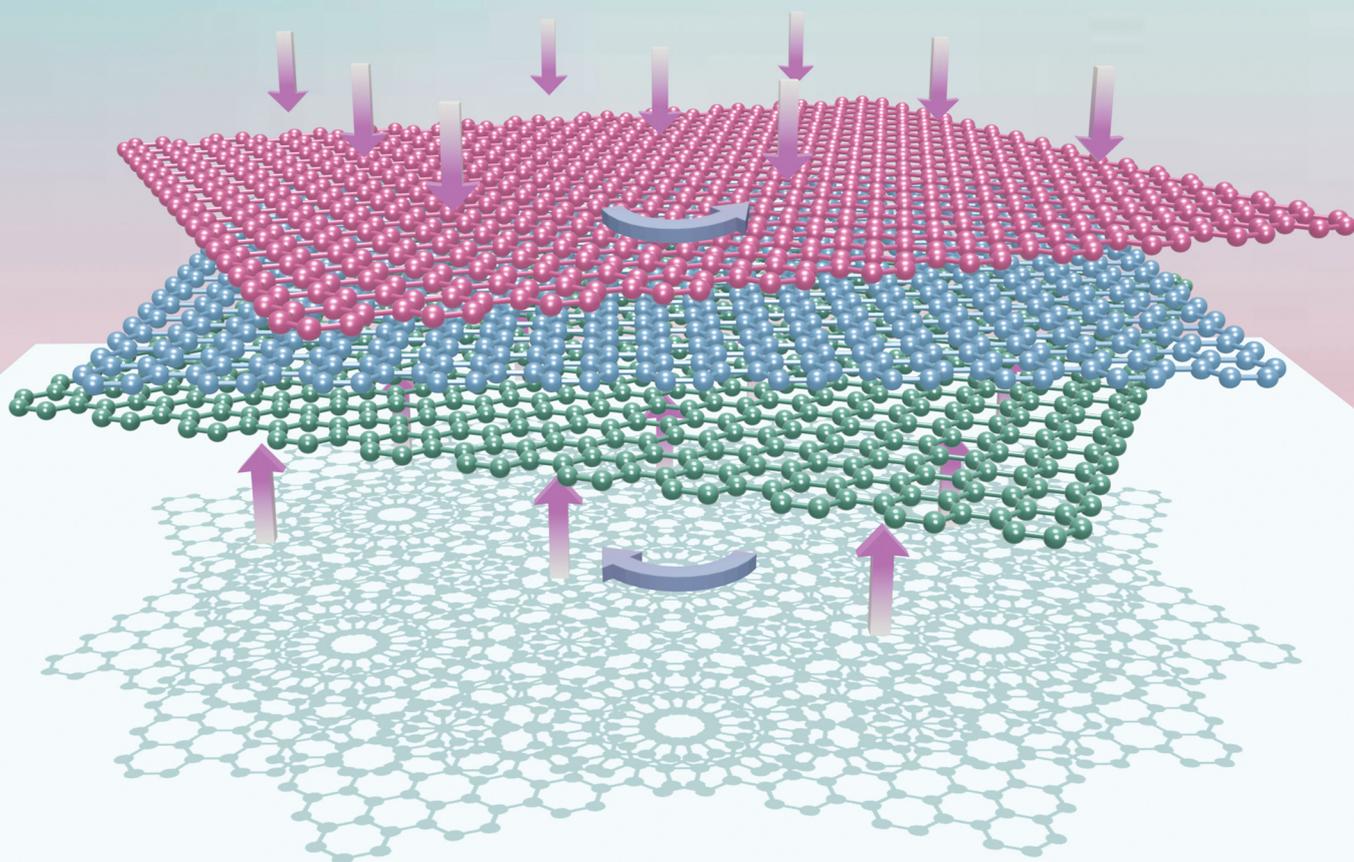
ROYAL SOCIETY OF CHEMISTRY

PAPER
Francisco Sánchez-Ochoa *et al.*
Electronic and optical properties in helical trilayer graphene under compression

PCCP Owner Societies

Check for updates

Electronic and optical properties in helical trilayer graphene under compression†

Ossiel Aguilar-Spíndola, (ID)[a] Alberto Rubio-Ponce, (ID)[b] Florentino López-Urías (ID)[c] and Francisco Sánchez-Ochoa (ID) *[a]

We built three periodic structures of high-angle helical trilayer graphene (hTLG-1, hTLG-2, and hTLG-3) with a relative interlayer rotation angle ($\theta = 21.78°$) and different initial vertical stacking (locally a C_6 or C_3 symmetry) between consecutive bilayers. Two-dimensional (2D) real-space moiré patterns and the corresponding calculated diffraction patterns showed symmetry differences between the periodic structures. Once the atomic models were characterized in both real and reciprocal spaces, the electronic and linear optical properties of these hTLG systems were studied using density functional theory (DFT) calculations and interlayer compression (δ) as an additional degree of freedom. The electronic band structures and total density of states (DOS), the real part of in-plane 2D linear optical conductivity ($\mathrm{Re}[\sigma_{2D}]$), and optical absorption (α) properties were studied. The electronic properties revealed an electron–hole asymmetry around the Fermi energy at different δ values, although strong hole localization at high compression ($\delta \leq -19\%$) was obtained. Indeed, we found high $\mathrm{Re}[\sigma_{2D}]$ values: $\mathrm{Re}[\sigma_{2D}(\hbar\omega = 90 \text{ meV})] \sim 9.5\sigma_0$, $\mathrm{Re}[\sigma_{2D}(\hbar\omega = 65 \text{ meV})] = 18\sigma_0$, and $\mathrm{Re}[\sigma_{2D}(\hbar\omega = 170 \text{ meV})] = 10\sigma_0$ for the hTLG-1, hTLG-2 and hTLG-3, respectively, when $\delta = -21.6\%$. $\sigma_0 = e^2\pi/2h$, is the optical conductivity of monolayer graphene. In addition, an α enhancement in the visible spectrum was obtained. These results demonstrate the relevance of the initial vertical stacking and interlayer compression on the electronics and optics of hTLG superlattices.

1. Introduction

Graphene has been a cornerstone in the field of nanomaterials since its discovery that is known for its extraordinary electrical, mechanical, and thermal properties. The discovery of superconductivity in twisted bilayer graphene (tBLG), among other interesting phenomena such as correlated insulating states, orbital magnetism, and resonating valence bond states,[1–7] has sparked interest in exploring other geometric arrangements of graphene. The aforementioned physical phenomena have been ascribed to nearly flat electronic bands positioned at the Fermi energy.[8–11] Subsequently, similar phenomena were observed in twisted trilayer graphene (tTLG)[12–15] and twisted multilayer graphene (tMLG) systems.[16,17] Some researchers believe that these systems represent the beginning of a new era in materials science,[18,19] since these layered and twisted van der Waals homostructures belong to a new group of quantum nanomaterials. Currently, the configuration of multilayered systems with properties different from those of monolayer graphene is one of the current research topics. Among these configurations, helical trilayer graphene (hTLG) is a fascinating structure owing to its unique electron correlation and optical properties.[20–23] The hTLG consists of three graphene layers, with the top and bottom layers twisted relative to the middle layer at specific angles. A variant of three-layer graphene, hTLG, introduces an additional degree of freedom, namely, helical layering. This arrangement creates a periodic moiré pattern, which becomes a new degree of freedom that allows us to manipulate the electronic band structures and optical response such that it is not involved in either the monolayer or the bilayer.

In twisted graphene systems, the interlayer rotation angle (θ) is an adjustable parameter for tuning physical properties. However, from an *ab initio* perspective, the study of electronic properties, for example, for twisted systems with low or marginal angles is limited by practical computational resources. This is because the low θ values imply the presence of several thousands atoms.[24] Hence, as an alternative to θ, external

[a] *Departamento de Materia Condensada, Instituto de Física, Universidad Nacional Autónoma de México, Apartado Postal 20-364, Cd. de México, C.P. 01000, Mexico. E-mail: fsanchez@fisica.unam.mx*

[b] *Departamento de Ciencias Básicas, Universidad Autónoma Metropolitana – Azcapotzalco, Av. San Pablo no. 420, Col. Nueva el Rosario, C.P. 02128, Ciudad de México, Mexico*

[c] *División de Materiales Avanzados, Instituto Potosino de Investigación Científica y Tecnológica, Camino a la Presa San José 2055, Col. Lomas 4a Sección, San Luis Potosí, S.L.P 78216, Mexico*

† Electronic supplementary information (ESI) available: Atomic models of primitive cells and twisted bilayer systems with different initial stacking, general information on the number of carbon atoms and interlayer angles in helical systems, comparison between two helical systems with different angles, and electronic band structures with different approximations. See DOI: https://doi.org/10.1039/d5cp00337g

This journal is © the Owner Societies 2025

Phys. Chem. Chem. Phys., 2025, **27**, 11541–11550 | 11541

hydrostatic pressure is a prominent auxiliary variable in experimental and first-principles studies.[25,26] The effects of pressure on the Fermi level position, charge carrier mobility, topological transitions, and electronic phase transitions in tBLG have been demonstrated in recent theoretical and experimental studies.[2,27-35] By applying external pressure to the hTLG structure, the interlayer distance can be set, which significantly affects the electronic interactions between the layers. This ability to tailor the effects of pressure is suitable for controlling the electronic and optical properties of hTLG systems, thus turning them into versatile platforms for studying various phenomena ranging from superconductivity and magnetism to advanced optical electronics. Nonetheless, it is worth noting that as in bulk-graphite with AA or AB (Bernal) stacking, the low-energy electronic properties are different[36]; moreover, the low-energy spectrum is different in tBLG systems because of the initial vertical stacking.[37,38] Vertical stacking in tBLG systems is termed sub-lattice exchange parity with C_6 or C_3 rotation symmetry. The electronic and optical properties of high-angle tBLG have a sublattice exchange parity dependence as shown by Talkington and Mele in ref. 39 and 40.

In this paper, we present a theoretical study of the electronic and optical properties of high-angle commensurate hTLG using total energy density functional theory (DFT) calculations. We built a minimal periodic structure of hTLG with $\theta = 21.78°$ between consecutive bilayers and counter-clockwise helicity. Here, we consider the interlayer compression, δ, and the local sublattice-exchange parity C_6 or C_3,[37-40] as two additional degrees of freedom to tune the electronic and optical properties of the hTLG. This shows that: (1) the external pressure is a versatile control knob for tuning the electronic properties instead of θ, and (2) the initial sublattice exchange parity between layers is useful for differentiating among hTLG structures and tuning the electronic and optical properties at high pressure. The outline of this paper is as follows: the computational methodology is presented in Section 2, the results and discussion are presented in Section 3, and the conclusions of the results are provided in Section 4.

2. Computational methodology

The ground-state structural, electronic, and optical properties were calculated using the DFT formalism implemented in the SIESTA code.[41,42] The electron exchange–correlation effects were described with a generalized gradient approximation (GGA) following the Perdew–Burke–Ernzerhof (PBE) parametrization,[43] meanwhile, electron–ion interactions were treated with norm-conserving Trouiller-Martins pseudopotentials.[44] Because SIESTA uses a linear combination of numerical pseudoatomic orbitals (LCAO), we employed an optimized single-ζ polarized (SZP) basis set to expand the Kohn–Sham wavefunctions with an energy mesh-cutoff of 350 Ry. The structural parameters and forces were converged using a Γ-centered $27 \times 27 \times 1$ Monkhorst–Pack k-grid.[45] An electronic temperature of 10 K was used for Fermi surface broadening. The atomic positions were optimized until the residual forces were 5 meV Å^{-1} or less, with a threshold value for electronic self-consistency of 10^{-4} eV. To simulate hTLG as a slab, we employed the supercell (SC) method with a vacuum space of 20 Å between adjacent graphene monolayers. The atomic models were visualized using VESTA software.[46]

3. Results and discussion

3.1. Real and reciprocal space

The optimized hexagonal crystal structure of monolayer graphene is represented by the following three optimized lattice parameters:

$$a_G = 2.46 \text{ Å}, \ b_G = 2.46 \text{ Å}, \ c_G = 30.00 \text{ Å},$$
$$\alpha = 90°, \ \beta = 90°, \ \gamma = 120°. \quad (1)$$

To build the hTLG systems with local even (C_6 in-plane axis rotation symmetry) or odd (C_3 in-plane axis rotation symmetry) initial stackings in the AA regions of moiré patterns, we employed Nook-iin software[47] with the following two carbon atomic bases in fractional coordinates:

$$C_A = (1/3, 2/3, 0), \ C_B = (2/3, 1/3, 0),$$
$$C_{A'} = (1/3, 2/3, 0), \ C_{B'} = (0, 0, 0), \quad (2)$$
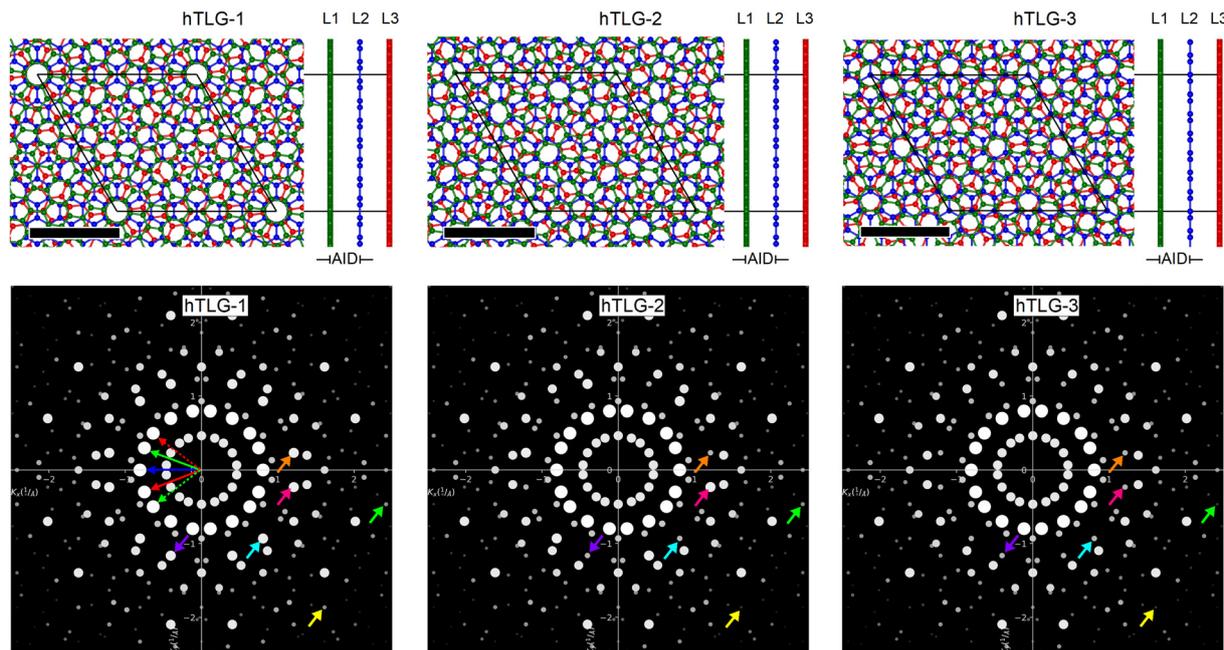
and the procedure described in ref. 24, 26, 48 and 49 for the highest commensurable angle of $\theta = 21.78°$. Fig. S1 of the ESI,† shows real space representations of the graphene monolayer with the atomic basis defined in eqn (2). The tBLG with different AA, AB or BA regions owing to different initial stackings are shown in Fig. S2 of the ESI.† The green, blue, and red spheres in Fig. 1 represent the top, middle, and bottom graphene monolayers, respectively. We labeled three different atomic configurations: hTLG-1, hTLG-2, and hTLG-3, which correspond to even–even, even–odd, and odd–odd parities between consecutive pairs of layers. For example, the hTLG-1 system has an even parity between the green and blue layers, and the same even parity is maintained between the blue and red layers. This was observed in the regions with AA stacking at the corners of the hexagonal lattice, as shown in Fig. 1 and Fig. S3(a) of the ESI.† VESTA software can be used to obtain the lattice vectors and atomic basis of the three layers using the following transformation matrix:[48,49]

$$P(m,n) = \begin{pmatrix} m & n & 0 \\ -n & m+n & 0 \\ 0 & 0 & 1 \end{pmatrix}. \quad (3)$$

The m and n integer values used in eqn (3): $P_G(5,3)$, $P_B(7,0)$ and $P_R(8, -3)$ for the green, blue, and red layers, respectively, were obtained using Nook-iin software.[47] These three transformation matrices ensure the same θ value between consecutive bilayers. Thus, the transformation matrices are as follows:

$$P_G = \begin{pmatrix} 5 & 3 & 0 \\ -3 & 8 & 0 \\ 0 & 0 & 1 \end{pmatrix}, \ P_B = \begin{pmatrix} 7 & 0 & 0 \\ 0 & 7 & 0 \\ 0 & 0 & 1 \end{pmatrix}, \ P_R = \begin{pmatrix} 8 & -3 & 0 \\ 3 & 5 & 0 \\ 0 & 0 & 1 \end{pmatrix}. \quad (4)$$

11542 | *Phys. Chem. Chem. Phys.*, 2025, **27**, 11541–11550

This journal is © the Owner Societies 2025

Fig. 1 Top panels: Top and side views of hTLG systems with $\theta = 21.78°$ between consecutive bilayers. Black lines delimit the periodic cell. Black scale bar, 10 Å. Green, blue, and red spheres represent carbon atoms at the top (L1), middle (L2), and bottom (L3) graphene layer. The average interlayer distance (AID) is defined between the L1 and L2 graphene layers. Bottom panels: Calculated diffraction patterns projected on the (001) plane. Small colored arrows denote diffraction spots for comparison among three structures. While large red, blue and green arrows pointing from the origin are steers to observe different relative orientations between consecutive layers. All the white spots are normalized to the diffraction spot with the second highest intensity. Scale in Å^{-1}.

To construct the hTLG-1 system shown in Fig. 1, we used the lattice parameters in eqn (1), the first atomic bases C_A and C_B of eqn (2), and the transformation matrices in eqn (4) for every graphene layer in the VESTA software.[46] For the hTLG-2 system, we used the same lattice parameters as those in eqn (1), but with the C_A and C_B, C_A and C_B, and $C_{A'}$ and $C_{B'}$ atomic bases for the red, blue, and green layers of eqn (2) and the same transformation matrix for each system in eqn (4). The last configuration hTLG-3 was set with the C_A and C_B, $C_{A'}$ and $C_{B'}$, and C_A and C_B basis for the red, blue, and green layers in eqn (2), respectively, and the transformation matrix for each graphene layer in eqn (4). Using the P matrices in eqn (4), the lattice parameter of hTLG is $a_{hTLG} = \sqrt{|\det P|} \times a_G = 7 \times a_G$. Additionally, the $|\det P|$ yields the same number of graphene unit cells inside the SC, that is, 49 unit cells. The three structures shown in Fig. 1 comprise 294 carbon atoms. These are the smallest helical structures that can be studied using DFT formalism implemented in the SIESTA package. We built other periodic structures with angles ranging from 8° to 30°, but the number of atoms was greater than 1800. See the plot and table in Fig. S3(b) of the ESI.† These structures are challenging to study numerically with DFT especially the physical properties like the linear optical properties as the optical conductivity, σ_{2D}. Thus, our study focused on the smallest periodic trilayer graphene owing to the limited computational resources. Notably, the transformation matrices in eqn (4) can be used to build other periodic helical homostructures. For example, hexagonal boron nitride (hBN) and transition metal

dichalcogenides (TMDCs) layers. Indeed, this hTLG system is a minimally twisted, helical, and commensurable structure with null strain along the lattice vectors, as a result of using the Nook-iin software.[47]

With the atomic models forming moiré patterns in the real space in Fig. 1, owing to the superposition of the three monolayers, the observation of symmetries or local differences between structures is rather difficult. An alternative to discerning the possible symmetries in these hTLG structures is their reciprocal space representation as diffraction patterns (see the bottom panels in Fig. 1). Hence, we plot the reciprocal space of periodic hTLG systems; for each reciprocal lattice point, we calculate its intensity value, I, using the corresponding structure factor, F_{hkl}, as $I = |F_{hkl}|^2$. F_{hkl} is a function of the atomic form factor, $f_m(|\vec{G}|)$. For every reciprocal lattice point,

$$F_{hkl} = \sum_{m\,\text{atoms}} f_m\left(\left|\vec{G}\right|\right) e^{i2\pi(hx_m+hy_m+lz_m)}, \quad \text{with}$$

$$f_m\left(\left|\vec{G}\right|\right) = \sum_{i=1}^{4} a_i e^{\left(-b_i\left(\frac{|\vec{G}|}{4\pi}\right)^2\right)} + c, \quad (5)$$

where h, k, and l are the Miller integer indices, and x_m, y_m, and z_m are the fractional coordinates of the atomic basis. We considered that the electron density is spherically symmetric such that the value of the Fourier transform, f_m, solely depends on the distance, $|\vec{G}|$, from the origin in reciprocal space.[50] The constants a_i, b_i, and c for carbon atoms, $a_1 = 2.31$, $b_1 = 20.8439$,

$a_2 = 1.02$, $b_2 = 10.2075$, $a_3 = 1.5886$, $b_3 = 0.5687$, $a_4 = 0.865$, $b_4 = 51.6512$ and $c = 0.2156$ were taken from ref. 50. The size symbol of the circles is proportional to the I of the spots in Fig. 1. The I value for all the peaks was normalized to the second maximum intensity value using 100 Miller indices. Because the diffraction spots are represented in 2D, we set the $l = 0$ in eqn (5), to avoid the slab thickness problem in the hTLG system.

In general, at the equilibrium average interlayer distance (AID) of $AID_0 = 3.235$ Å, the diffraction patterns show a set of 18 small spots surrounding the origin (Γ point) in reciprocal space. This is because there are three graphene layers with six rotational symmetries. The second set of diffraction spots is more intense than that of the first set, but it reveals an interlayer relative orientation difference between the consecutive layers. This is depicted by the large colored arrows in the hTLG-1 configuration, starting from the origin. The interlayer angles between red and blue and the blue and green arrows are the same, $\theta = 21.78°$. However, the angle between the dashed green arrow and its neighboring red arrow (equal to the angle between the green arrow and its neighboring dashed red arrow) is small and equal to $(360° - 12 \times 21.78°)/6 = 16.44°$. A smaller interlayer angle lies between the outermost green and red graphene layers. To be precise, an interlayer angle of 16.44° is also commensurable and is the same angle found when a graphene bilayer is built with integer pairs $(m,n) = (5,3)$ as in ref. 24. The difference in the relative orientation between the blue and red layers and the green and red layers was observed by the arc length formed by relating the spots indicated by arrows. The space group for each system was obtained by using the PYMATGEN SPGLIB module.[51] The calculated space groups for the hTLG-1, hTLG-2, and hTLG-3 systems were $P622$ (space group no. 177), $P3$ (space group no. 143), and $P312$ (space group no. 149), respectively. Thus, their symmetric Patterson representation are $P6/mmm$ (hTLG-1), $P\bar{3}$ (hTLG-2), and $P\bar{3}1m$ (hTLG-3). From the highest to the lowest symmetry configuration, hTLG-1 → hTLG-3 → hTLG-2, the in-plane symmetry decreased; that is, the symmetry in 2D was $P6/mmm$, $\bar{3}1m$ and $\bar{3}$ for hTLG-1, hTLG-3, and hTLG-2, respectively. There were twelve, three and six

symmetry operations in the following order: hTLG-1, hTLG-2, and hTLG-3. From the calculated space groups, we can observe that, in general, hTLG-1 has a six-fold rotation axis with a symmetry plane normal to it and another not so, whereas hTLG-2 has a three-fold inversion axis alone, and hTLG-3 has a three-fold inversion axis with a symmetry plane not normal to it in 3D. It should be noted that the hTLG-2 configuration lost three σ mirrors in 2D compared to hTLG-1, as shown by the asymmetry between the two spots signaled by the small orange and pink arrows near the positive k_x-axis. The spots indicated by the purple, cyan, and orange arrows were equivalent; however, these sets of spots were not equivalent to those indicated by the pink, yellow, and green arrows, among others.

3.2. Density of states and band structures

Interlayer compression, δ, is considered an alternative clean knob to the relative interlayer orientation, θ, for tuning electronic properties around the Fermi energy.[2,25,26,52,53] Therefore, we used δ to tune the electronic and optical properties of hTLG with different initial stackings. To simulate the compression effect in hTLG, we left the x and y components of the atomic positions free to relax at different AID values, while the z-coordinate was fixed. AID can be mapped to δ as $\delta = (AID - AID_0)/AID_0 \times 100\%$. Thus, δ varied from 0% to $\sim -25\%$ with $AID_0 = 3.235$ Å. Fig. 2 shows the color map plots of the total density of states (DOS) for different AID (or δ) values around the Fermi energy. At first glance, the total DOS plots show electron–hole asymmetry. This is noticeable by the energy splitting of the first van Hove singularity (vHS) positioned at -1 eV (for holes) compared with the corresponding vHS at 1.2 eV (for electrons) when $\delta = -1.1\%$, in the three configurations. In addition, the first two lowest-energy vHSs approached the Fermi energy at different δ rates. Large asymmetric differences were observed at $\delta < -10\%$. For high δ (or low AID) values, the hole vHS approaches the Fermi energy and leads to a localized state in the hTLG-2 and hTLG-3 configurations. Hence, the total DOS shows how the initial local sub-lattice exchange parity matters and can lead to a low-energy asymmetry near the Fermi energy. This electron–hole asymmetry may affect
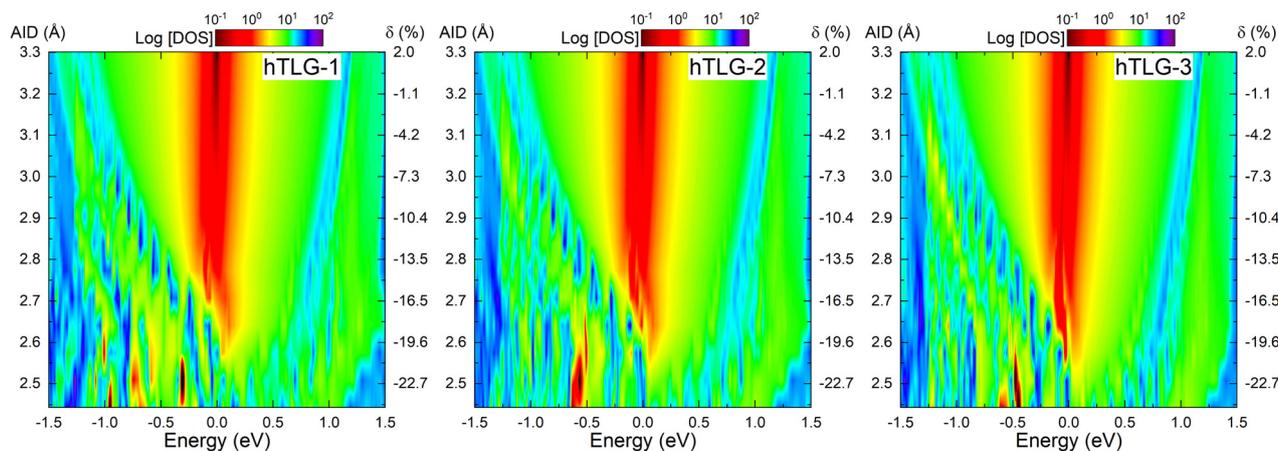

Fig. 2 Log-scale total density of states (DOS) as a function of energy and average interlayer distance (AID) or equivalently as an interlayer compression (δ). The Fermi level is set to 0 eV.

11544 | *Phys. Chem. Chem. Phys.*, 2025, **27**, 11541–11550

This journal is © the Owner Societies 2025

the conductor and optical properties, and the physical properties could be very different from those of tBLG systems. We want to stress the possibility of a magnetic phase transition, such as ferromagnetic or antiferromagnetic states, in the hTLG-2 and hTLG-3 systems because of the high and narrow peaks positioned at the Fermi energy in the total DOS.[52] In these plots, the Dirac point (DP) was identified as a narrow dark energy region for AID > 3.1 Å. Finally, for AID $\simeq$ 2.5 Å several bandgaps can be observed in the valence regime solely for hTLG-1 configuration. We can provide a rough estimation of the applied external pressure by employing the results of ref. 26 based on DFT calculations of twisted and periodic multilayered graphene structures. With A = 14.42 GPa and β = 9.54 (being average values between even and odd bilayer graphene with an interlayer angle of 21.8°), in the expression $P = A(e^{-\beta\delta} - 1)$; we calculate a pressure value of P = 51.21 GPa if the compression is $\delta = -21.6\%$. We want to stress that the van der Waals interactions with the Klimeš–Bowler–Michelides (KBM) approximation[54] have a negligible effect on the electronic structure at high pressures compared to the GGA (PBE) functional, as shown in Fig. S4 of the ESI.†

The band 'folding' is a common issue in electronic structure calculations for periodic systems with many primitive cells forming a commensurate supercell like hTLG. This band folding mechanism gives a 'spaghetti' of electronic states piled up into mini Brillouin zone (BZ); and it frequently gives a difficult interpretation of physical interactions in a wide energy range when large supercells are studied. Standard supercell band structure calculations do not provide a direct comparison with angle-resolved photoemission spectroscopy (ARPES) measurements. Thus, an inverse approach to band folding can solve this problem to obtain an effective band structure showing physical interactions between layers and a more reliable comparison with experiments.[24,26,48,49] To apply the unfolding mechanism described in ref. 49 we first plotted the BZs, the irreducible BZs, and the high symmetry points of three graphene primitive cells in the reciprocal space of the hTLG supercell in Fig. 3. With this representation of reciprocal space, we can now determine the correspondence of high-symmetry points (K and K′) from primitive cells with those in the hTLG supercell (see inset in Fig. 3). Note that even when K′ of the green layer, K of the blue layer, and K′ of the red layer are positioned in the K′ of the hTLG supercell, the electronic states of the green and red layers do not interact directly. Instead they interact through the blue layer. Therefore, we applied the unfolding approach along the dashed blue k-path connecting $\Gamma \rightarrow K \rightarrow M \rightarrow \Gamma$ points to calculate the spectral weight $W(k, I)$ for each eigenstate, k is the wavevector and I is the band index, which is solved for each layer. Further details regarding the unfolding approach can be found in ref. 24, 26, 48 and 49.

We chose the hTLG systems with AID = 3.03 Å ($\delta \sim -6.37\%$) to apply the unfolding method because these systems do not show large differences in the total DOS in Fig. 2. The results in Fig. 4 show that the electronic states around the Fermi energy are due to the blue layer, which resembles the linear dispersion of Dirac cones. For energies lower than −1 eV, several discontinuities in the band structure were observed along the K–M
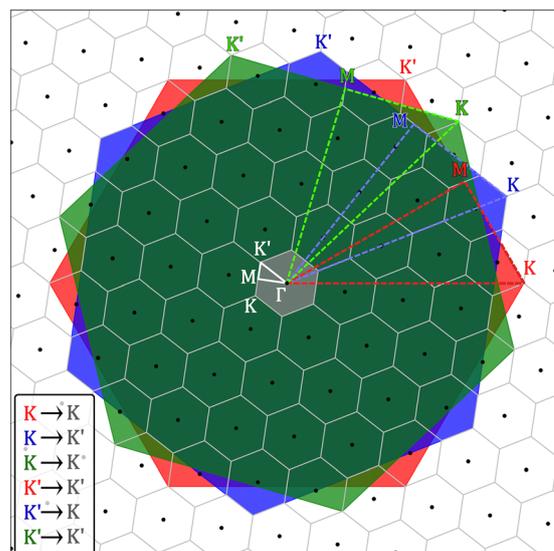

Fig. 3 Reciprocal space of periodic hTLG with θ = 21.78°. Lattice points represented with black dots are surrounded by gray hexagonal mini BZs. In the same supercell reciprocal space, the first BZs of graphene primitive cells and their corresponding irreducible BZs are plotted with green, blue and red colors. High symmetry points for the mini BZ are colored with light gray.

path, where the electronic bands originated mainly from the outer green and red graphene layers. Three electronic bands were found for the K $\rightarrow$ Γ and M $\rightarrow$ Γ paths, from which the darker green band represents hybridization between the outer red (50%) and green (50%) layers. The outer bands near the Γ point (dark blue) have contributions from the red (25%), blue (50%), and green (25%) layers. We have identified less-dispersive electronic states just at the M point and −1 eV with gray color, which means an equal proportion ($\sim$33.33%) of the three graphene layers. These last electronic states deserve further study because of the delocalization occurring along the direction perpendicular to the layers, whereas a high in-plane confinement is observed by the localized states.[24] This could guide experimentalists to pursue the synthesis and in-depth characterization of three-dimensional (3D) twistronics in quantum layered materials.[55]

3.3. Optical conductivity and absorbance

Because the hTLG systems were simulated as slabs of stacked graphene layers and a vacuum space within the supercell method, the macroscopic dielectric function, $\varepsilon_{3D}(\omega)$, of the hTLG material can not be defined. Hence, to avoid the thickness problem, the 2D in-plane optical conductivity, $\sigma_{2D}(\omega)$, is used instead of $\varepsilon_{3D}(\omega)$[56] for linear optical property calculations. Note that the constraint of normal incidence of polarized light on the sample is considered. The relationship between $\varepsilon_{3D}(\omega)$ and $\sigma_{3D}(\omega)$ is as follows:

$$\varepsilon_{3D}(\omega) = 1 + \frac{i}{\varepsilon_0 \omega} \sigma_{3D}(\omega), \tag{6}$$

where ε_{3D} is ε in the bulk, ε_0 is the vacuum permittivity and σ_{3D} is the 3D bulk optical conductivity. Alternatively, $\sigma_{3D}(\omega) = i[1 - \varepsilon_{3D}(\omega)]\varepsilon_0\omega$.

This journal is © the Owner Societies 2025

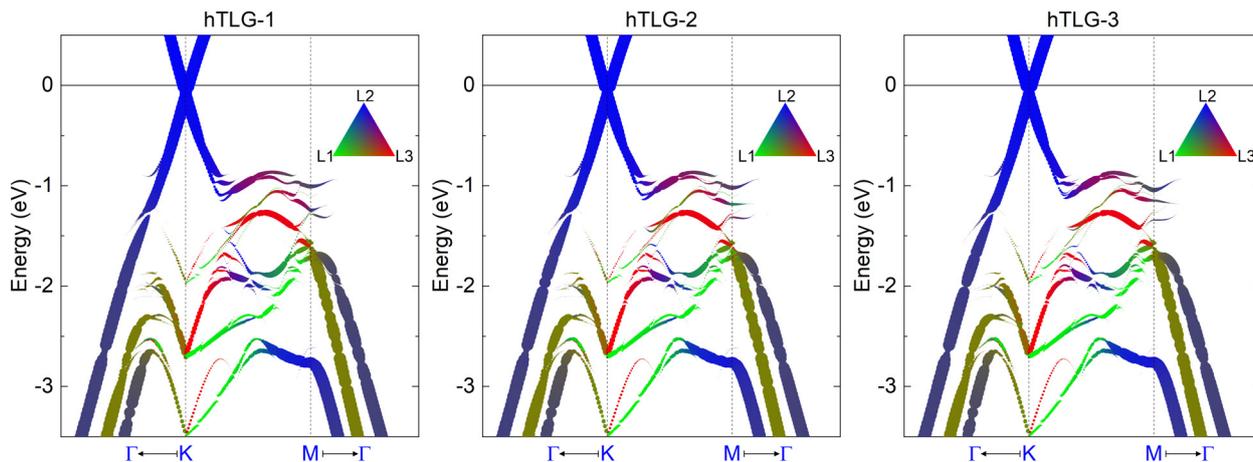*Phys. Chem. Chem. Phys.*, 2025, **27**, 11541–11550 | **11545**

Fig. 4 Unfolded band structures calculated along the high symmetry k-path for blue primitive cell. Along the same k-path, the electronic contributions from green and red layers are plotted. The normalized spectral weight, $W(k, l)$, for the red, blue, and green layers are rescaled to integer values (from 0 to 255), to obtain a triad value for plotting each electronic state with circle symbols, whose size and color (in RGB format) are proportional to the $W(k, l)$. The Fermi energy is set to 0 eV. The color triangle is defined to represent the L1, L2 and L3 layer contribution similar to Fig. 1.

The $\sigma_{3D}(\omega)$ can be related to the $\sigma_{2D}(\omega)$ through the slab thickness L, as follows:[57,58]

$$\sigma_{2D}(\omega) = L\sigma_{3D}(\omega). \tag{7}$$

Finally, the real part of σ_{2D} (also known as the longitudinal conductivity component), $\text{Re}[\sigma_{2D}(\omega)]$, was calculated instead of $\varepsilon(\omega)$,[59,60] which is equivalent to the imaginary part of ε_{3D}, $\text{Im}[\varepsilon_{3D}]$, and incorporates the light absorption mechanism in 2D materials. The $\text{Im}[\sigma_{2D}(\omega)]$ term is similar to the $\text{Re}[\varepsilon_{3D}(\omega)]$ term and is related to the refractive index. Thus, once the ground state electronic properties of the hTLG systems were calculated for several δ values, we proceeded to calculate the real, $\varepsilon_1(\omega)$, and imaginary, $\varepsilon_2(\omega)$, parts of the frequency-dependent complex dielectric function $\varepsilon(\omega)$. For this purpose, an electric field was applied along the x-direction to determine $\varepsilon_1(\omega)$ and $\varepsilon_2(\omega)$ within the single-particle approximation neglecting the Drude contributions (intraband transitions) for low energies. Thus, only the direct ($\mathbf{q} \rightarrow 0$) electronic interband transitions were calculated.

Fig. 5 shows the $\text{Re}[\sigma_{2D}]$ values for the three different hTLG systems as a function of δ. The uncompressed systems exhibited a sharp peak in $\hbar\omega \sim 4.2$ eV due to transitions between electronic states located at the van Hove singularities (around the M point in the band structure) of graphene monolayer, meanwhile $\text{Re}[\sigma_{2D}] \approx 3\sigma_0$ (with $\sigma_0 = e^2\pi/2h$ the conductance quantum) at low energies. For most incident photon energies, a significant enhancement in $\text{Re}[\sigma_{2D}]$ is observed when the interlayer compression, δ, increases. However, a contrary effect is observed around $\hbar\omega \sim 4.2$ eV, because $\text{Re}[\sigma_{2D}]$ dropped with the interlayer compression strength. Notice that, a peak splitting is observed with reduced intensities for the minimal compression strength (see the more intense blue lines), for $\hbar\omega \sim 4.2$ eV. At low photon energies, the compressed trilayers exhibit the most remarkable increase in $\text{Re}[\sigma_{2D}]$; see the bottom panels in Fig. 5. For a high compression value of $\delta \approx -21.6\%$, the $\text{Re}[\sigma_{2D}]$ increased by up to $\sim 9.5\sigma_0$ ($\hbar\omega = 90$ meV),

$18\sigma_0$ ($\hbar\omega = 65$ meV), and $10\sigma_0$ ($\hbar\omega = 170$ meV) for the hTLG-1, hTLG-2, and hTLG-3 systems, respectively. Furthermore, for the low-photon energy regime and intermediate compression values, the hTLG-1 system exhibited smaller values of $\text{Re}[\sigma_{2D}]$ than σ_0, as shown in Fig. 5. The high $\text{Re}[\sigma_{2D}]$ values at low incident photon energies can be ascribed to direct electron transitions in the corresponding SC band structure, as shown in Fig. 6. The colored band structures in Fig. 6 show the contribution or mixing of each layer for every electronic state, in a format similar to that in Fig. 4. The possible direct band-to-band electronic transitions are indicated by the vertical red arrows, leading to the maximum conductivity values indicated by the small blue arrows in Fig. 5. Even when there are a large number of vertical electronic transitions, as shown in Fig. 6, the optical transition rate probability, which is a function of the average dipole moment operator, should be considered to discard electronic transitions with a null transition probability. It is important to note that the hTLG-2 structure with lower $P\bar{3}$ symmetry has a maximum $\text{Re}[\sigma_{2D}] = 18\sigma_0$ value at a high δ compression.

The enhancement of $\text{Re}[\sigma_{2D}]$ for energies less than 0.5 eV, and in the energy range between ~ 1.5 to ~ 3.5 eV, is a clear fingerprint of an increase in optical absorbance, A, for the incident perpendicular light to the system because:[61]

$$A = \frac{4\pi}{c}\text{Re}[\sigma_{2D}], \tag{8}$$

where c is the speed of light. On the other hand, we also calculated the in-plane linear optical absorption coefficient, $\alpha(\omega)$, from the $\varepsilon_1(\omega)$ and the $\varepsilon_2(\omega)$ parts as follows:

$$\alpha(\omega) = \frac{\sqrt{2}\omega}{c}\left[\sqrt{\varepsilon_1^2 + \varepsilon_2^2} - \varepsilon_1^2\right]^{\frac{1}{2}}. \tag{9}$$

Fig. 7 shows the calculated α values for the different δ values. The rainbow window indicates the photon energy in the visible range. Generally, an α enhancement is observed as the interlayer compression increases. However, around $\hbar\omega \sim 4.2$ eV, the
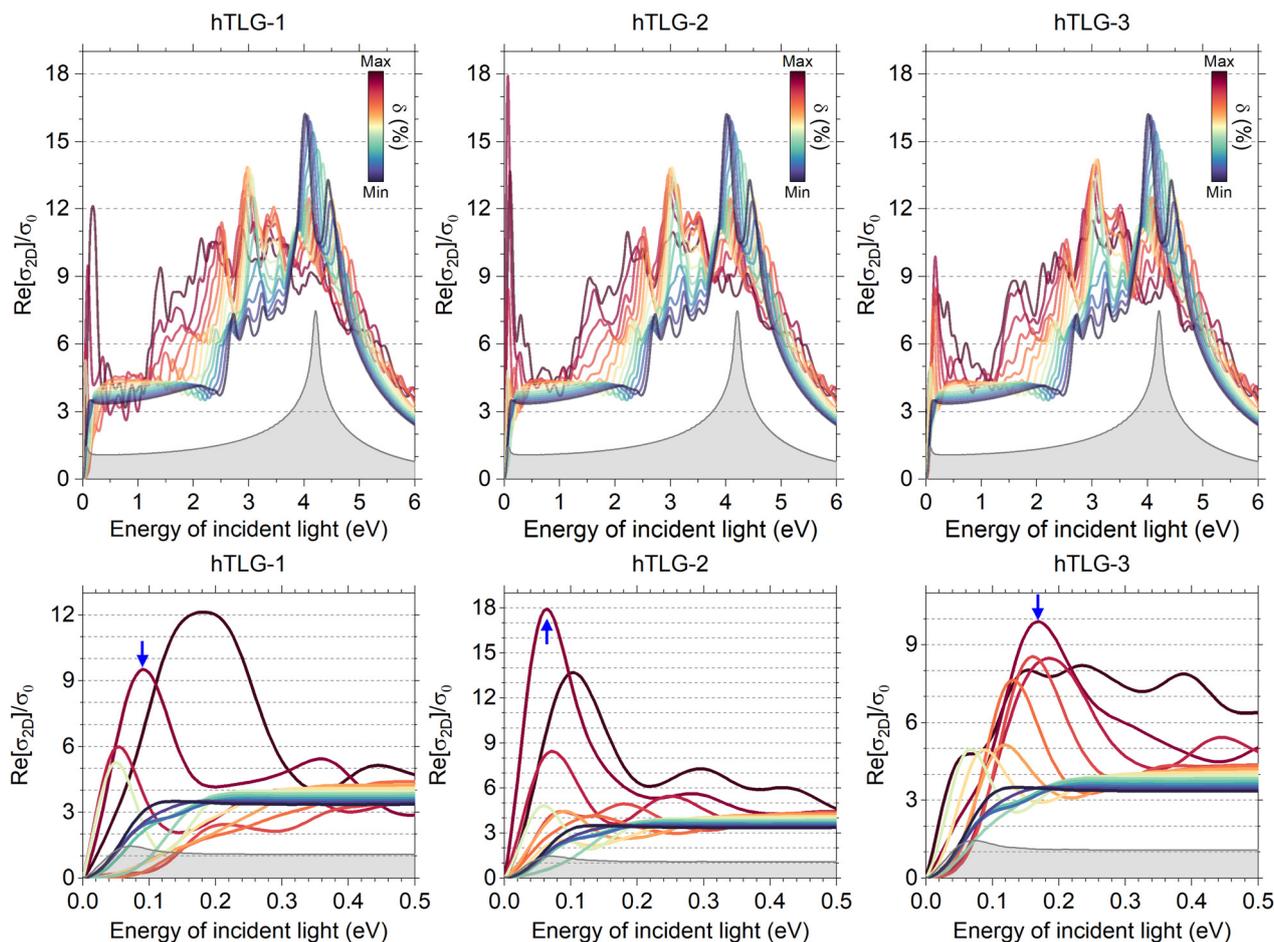
Fig. 5 Top panels: Real part of in-plane longitudinal optical conductivity, Re[σ_{2D}], calculated for several δ values in a wide energy range of incident light. Bottom panels: The same as the top panels but for a lower incident photon energy. Blue arrows point to high peaks in Re[σ_{2D}] when $\delta = -21.6\%$, for comparison purposes. To compare between results, the Re[σ_{2D}] of the graphene monolayer is plotted with gray color. $\sigma_0 = e^2\pi/2h$.
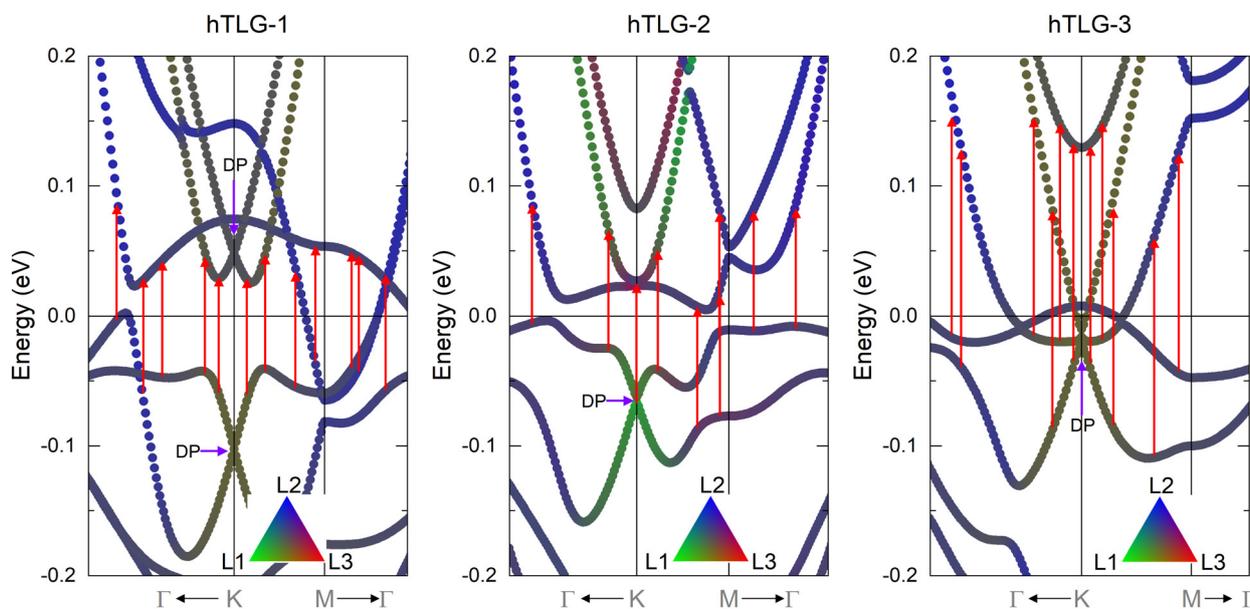

Fig. 6 Supercell electronic band structures calculated along the paths defined by the high symmetry points in Fig. 3. The high compression value is $\delta = -21.6\%$. Different layer contributions in the band structure are plotted with green (layer 1), blue (layer 2) and red (layer 3). Dirac points (DP) observed below zero eV means an n-doping effect. Vertical dashed red arrows indicate possible direct electron transitions. The Fermi energy is set to 0 eV.
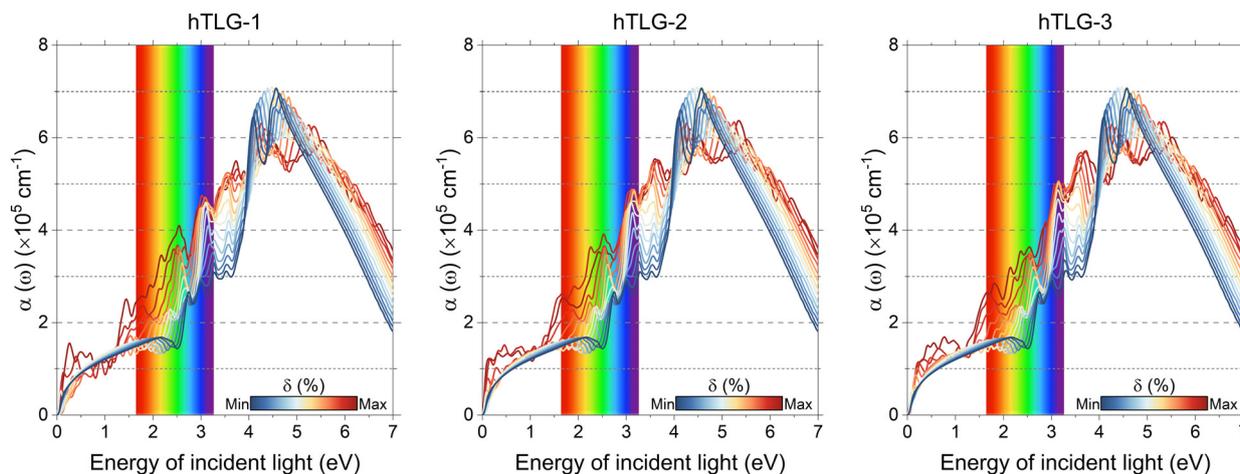
Fig. 7 In-plane linear optical absorption as a function of incident energy light and interlayer compression δ. The rainbow window delimit the energy range of visible electromagnetic spectrum.

compression strength suppresses the optical absorption as was observed for $Re[\sigma_{2D}]$, according with the experimental results of pressurized trilayer graphene.[62] Theoretical studies have reported that, for non-twisted multilayer graphene with Bernal stacking (ABAB...), the peak intensity in α increases as the number of graphitic layers do, and peak splitting at $\hbar\omega \sim 4.2$ eV emerges for trilayer and tetra-layered systems using out-of-plane polarization components of the electromagnetic field.[63] These results show that for low incident energies, <0.5 eV, the hTLG systems absorb perpendicular or parallel incident electromagnetic radiation differently, with more prominent perpendicular absorbance properties for the hTLG-2 structure, as shown in Fig. 5.

4. Conclusions

We studied the structural, electronic, and linear optical properties of three different periodic helical three-layer graphene (hTLG) systems using the total-energy DFT formalism. The interplay between the initial stacking (sub-lattice exchange parity) and interlayer distance for the tuning and enhancement of electronics and optics was addressed. Once the periodic atomic models were built, the diffraction patterns were calculated by considering the structure factor to detect the differences among the three configurations. Loss-symmetry behavior was observed from the highest (hTLG-1) to the lowest (hTLG-2) structure. Regarding the electronic structure, the total density of states is a tunable electronic property because it depends on the initial stacking fault and interlayer compression to achieve strongly localized asymmetric states around the Fermi level. The calculated effective band structures reveal clear interlayer interactions, such as hybridizations, and are likely in-plane confined but normal plane delocalized electronic states that connect the three layers. Finally, a substantial enhancement is observed in the linear optical properties, such as in the optical conductivity for lower energies (<1.5 eV) and in the optical absorbance mainly in the visible spectrum for practical optoelectronic applications. These theoretical results demonstrate the importance of initial vertical stacking and interlayer compression in the electronics and optics of hTLG superlattices, which can conveniently lead to experimentalists.

Author contributions

Ossiel Aguilar contributed to the investigation, software, resources, and validation of data. Alberto Rubio and Florentino López contributed to the conceptualization, formal analysis, investigation, supervision, validation, and visualization. Francisco Sánchez contributed to the conceptualization, formal analysis, supervision, investigation, and writing and editing of the original draft.

Data availability

Data will be made available from the corresponding author upon reasonable request.

Conflicts of interest

There are no conflicts to declare.

Acknowledgements

References

1 Y. Cao, V. Fatemi, S. Fang, K. Watanabe, T. Taniguchi, E. Kaxiras and P. Jarillo-Herrero, *Nature*, 2018, **556**, 43–50.
2 M. Yankowitz, S. Chen, H. Polshyn, Y. Zhang, K. Watanabe, T. Taniguchi, D. Graf, A. F. Young and C. R. Dean, *Science*, 2019, **363**, 1059–1064.

11548 | *Phys. Chem. Chem. Phys.*, 2025, **27**, 11541–11550

This journal is © the Owner Societies 2025

3 X. Lu, P. Stepanov, W. Yang, M. Xie, M. A. Aamir, I. Das, C. Urgell, K. Watanabe, T. Taniguchi and G. Zhang, *et al.*, *Nature*, 2019, **574**, 653–657.

4 P. Stepanov, I. Das, X. Lu, A. Fahimniya, K. Watanabe, T. Taniguchi, F. H. Koppens, J. Lischner, L. Levitov and D. K. Efetov, *Nature*, 2020, **583**, 375–378.

5 M. Oh, K. P. Nuckolls, D. Wong, R. L. Lee, X. Liu, K. Watanabe, T. Taniguchi and A. Yazdani, *Nature*, 2021, **600**, 240–245.

6 F. López-Urías, A. Rubio-Ponce, E. Muñoz-Sandoval and F. Sánchez-Ochoa, *J. Phys.: Condens. Matter*, 2024, **36**, 405802.

7 F. López-Urías, A. Rubio-Ponce, E. Muñoz-Sandoval and F. Sánchez-Ochoa, *Phys. Chem. Chem. Phys.*, 2024, **26**, 16955–16962.

8 J. M. B. Lopes dos Santos, N. M. R. Peres and A. H. Castro Neto, *Phys. Rev. Lett.*, 2007, **99**, 256802.

9 E. Suárez Morell, J. D. Correa, P. Vargas, M. Pacheco and Z. Barticevic, *Phys. Rev. B*, 2010, **82**, 121407.

10 G. Trambly de Laissardiere, D. Mayou and L. Magaud, *Nano Lett.*, 2010, **10**, 804–808.

11 R. Bistritzer and A. H. MacDonald, *Proc. Natl. Acad. Sci. U. S. A.*, 2011, **108**, 12233–12237.

12 J. M. Park, Y. Cao, K. Watanabe, T. Taniguchi and P. Jarillo-Herrero, *Nature*, 2021, **590**, 249–255.

13 Z. Hao, A. Zimmerman, P. Ledwith, E. Khalaf, D. H. Najafabadi, K. Watanabe, T. Taniguchi, A. Vishwanath and P. Kim, *Science*, 2021, **371**, 1133–1138.

14 H. Kim, Y. Choi, C. Lewandowski, A. Thomson, Y. Zhang, R. Polski, K. Watanabe, T. Taniguchi, J. Alicea and S. Nadj-Perge, *Nature*, 2022, **606**, 494–500.

15 X. Liu, N. J. Zhang, K. Watanabe, T. Taniguchi and J. Li, *Nat. Phys.*, 2022, **18**, 522–527.

16 J. M. Park, Y. Cao, L.-Q. Xia, S. Sun, K. Watanabe, T. Taniguchi and P. Jarillo-Herrero, *Nat. Mater.*, 2022, **21**, 877–883.

17 Y. Zhang, R. Polski, C. Lewandowski, A. Thomson, Y. Peng, Y. Choi, H. Kim, K. Watanabe, T. Taniguchi and J. Alicea, *et al.*, *Science*, 2022, **377**, 1538–1543.

18 E. Y. Andrei and A. H. MacDonald, *Nat. Mater.*, 2020, **19**, 1265–1275.

19 L. Balents, C. R. Dean, D. K. Efetov and A. F. Young, *Nat. Phys.*, 2020, **16**, 725–733.

20 C. Yang, J. May-Mann, Z. Zhu and T. Devakul, *Phys. Rev. B*, 2024, **110**, 115434.

21 T. Devakul, P. J. Ledwith, L.-Q. Xia, A. Uri, S. C. de la Barrera, P. Jarillo-Herrero and L. Fu, *Sci. Adv.*, 2023, **9**, eadi6063.

22 X. Zhang, K.-T. Tsai, Z. Zhu, W. Ren, Y. Luo, S. Carr, M. Luskin, E. Kaxiras and K. Wang, *Phys. Rev. Lett.*, 2021, **127**, 166802.

23 P. Moon, *Phys. Rev. B*, 2021, **104**, 115407.

24 F. Sánchez-Ochoa, A. R. Botello-Méndez and C. Noguez, *Phys. Rev. B*, 2021, **104**, 075430.

25 S. Carr, S. Fang, P. Jarillo-Herrero and E. Kaxiras, *Phys. Rev. B*, 2018, **98**, 085144.

26 F. Sánchez-Ochoa, A. Rubio-Ponce and F. López-Urías, *Phys. Rev. B*, 2023, **107**, 045414.

27 F. Munoz, H. P. O. Collado, G. Usaj, J. O. Sofo and C. A. Balseiro, *Phys. Rev. B*, 2016, **93**, 235443.

28 H. Shi, Z. Zhan, Z. Qi, K. Huang, E. V. Veen, J. Á. Silva-Guillén, R. Zhang, P. Li, K. Xie and H. Ji, *et al.*, *Nat. Commun.*, 2020, **11**, 1–7.

29 X. Lin, H. Zhu and J. Ni, *Phys. Rev. B*, 2020, **101**, 155405.

30 T. Zhang, C. Gao, D. Liu, Z. Li, H. Zhang, M. Zhu, Z. Zhang, P. Zhao, Y. Cheng and W. Huang, *Nano Lett.*, 2022, **22**, 5841–5848.

31 W. Xiong, L. Wen, X. Lv and Z. Li, *Phys. Lett. A*, 2023, **483**, 129048.

32 V. G. M. Duarte, D. R. da Costa, N. M. R. Peres, L. K. Teles and A. J. Chaves, *Phys. Rev. B*, 2024, **110**, 035405.

33 Y. Hou, J. Zhou, M. Xue, M. Yu, Y. Han, Z. Zhang and Y. Lu, *Small*, 2024, 2311185.

34 N. P. Kazmierczak, M. Van Winkle, C. Ophus, K. C. Bustillo, S. Carr, H. G. Brown, J. Ciston, T. Taniguchi, K. Watanabe and D. K. Bediako, *Nat. Mater.*, 2021, **20**, 956–963.

35 L. Ge, K. Ni, X. Wu, Z. Fu, Y. Lu and Y. Zhu, *Nanoscale*, 2021, **13**, 9264–9269.

36 A. H. Castro Neto, F. Guinea, N. M. R. Peres, K. S. Novoselov and A. K. Geim, *Rev. Mod. Phys.*, 2009, **81**, 109–162.

37 E. J. Mele, *J. Phys. D: Appl. Phys.*, 2012, **45**, 154004.

38 E. J. Mele, *Phys. Rev. B: Condens. Matter Mater. Phys.*, 2010, **81**, 161405.

39 S. Talkington and E. J. Mele, *Phys. Rev. B*, 2023, **108**, 085421.

40 S. Talkington and E. J. Mele, *Phys. Rev. B*, 2023, **107**, L041408.

41 P. Ordejón, E. Artacho and J. M. Soler, *Phys. Rev. B: Condens. Matter Mater. Phys.*, 1996, **53**, R10441.

42 J. M. Soler, E. Artacho, J. D. Gale, A. Garca, J. Junquera, P. Ordejón and D. Sánchez-Portal, *J. Phys.: Condens. Matter*, 2002, **14**, 2745.

43 J. P. Perdew, K. Burke and M. Ernzerhof, *Phys. Rev. Lett.*, 1996, **77**, 3865–3868.

44 N. Troullier and J. L. Martins, *Phys. Rev. B: Condens. Matter Mater. Phys.*, 1991, **43**, 1993.

45 H. J. Monkhorst and J. D. Pack, *Phys. Rev. B: Solid State*, 1976, **13**, 5188–5192.

46 K. Momma and F. Izumi, *J. Appl. Crystallogr.*, 2011, **44**, 1272–1276.

47 O. Aguilar-Espíndola, *OssielAg/Nook-iin: Nook'iin: First public version*, 2024, DOI: **10.5281/zenodo.14257397**.

48 F. Hidalgo, F. Sánchez-Ochoa and C. Noguez, *npj 2D Mater. Appl.*, 2023, **7**, 40.

49 F. Sánchez-Ochoa, F. Hidalgo, M. Pruneda and C. Noguez, *J. Phys.: Condens. Matter*, 2020, **32**, 025501.

50 P. J. Brown, A. G. Fox, E. N. Maslen, M. A. O'Keefe and B. T. M. Willis, in *International Tables for Crystallography Volume C: Mathematical, physical and chemical tables*, ed. E. Prince, Springer, Netherlands, 2004, vol. C, pp. 554–595.

51 A. Togo, K. Shinohara and I. Tanaka, *arXiv*, preprint, 2018, arXiv:1808.01590.

52 F. Yndurain, *Phys. Rev. B*, 2019, **99**, 045423.

53 M. Yankowitz, J. Jung, E. Laksono, N. Leconte, B. L. Chittari, K. Watanabe, T. Taniguchi, S. Adam, D. Graf and C. R. Dean, *Nature*, 2018, **557**, 404–408.

54 J. Klimeš, D. R. Bowler and A. Michaelides, *J. Phys.: Condens. Matter*, 2009, **22**, 022201.

55 F. Wu, R.-X. Zhang and S. Das Sarma, *Phys. Rev. Res.*, 2020, **2**, 022010.

56 T. Zhan, X. Shi, Y. Dai, X. Liu and J. Zi, *J. Phys.: Condens. Matter*, 2013, **25**, 215301.

This journal is © the Owner Societies 2025

Phys. Chem. Chem. Phys., 2025, **27**, 11541–11550 | 11549

57 L. Matthes, O. Pulci and F. Bechstedt, *New J. Phys.*, 2014, **16**, 105007.

58 L. Matthes, O. Pulci and F. Bechstedt, *Phys. Rev. B*, 2016, **94**, 205408.

59 A. Gusso, F. Sánchez-Ochoa and R. Esquivel-Sirvent, *Langmuir*, 2024, **40**, 10685–10694.

60 R. Esquivel-Sirvent, A. Gusso and F. Sánchez Ochoa, *Nanoscale Microscale Thermophys. Eng.*, 2023, **27**, 95–109.

61 K. F. Mak, L. Ju, F. Wang and T. F. Heinz, *Solid State Commun.*, 2012, **152**, 1341–1349.

62 F. Ke, Y. Chen, K. Yin, J. Yan, H. Zhang, Z. Liu, J. S. Tse, J. Wu, H.-K. Mao and B. Chen, *Proc. Natl. Acad. Sci. U. S. A.*, 2019, **116**, 9186–9190.

63 A. Kumar, G. Sachdeva, R. Pandey and S. P. Karna, *Appl. Phys. Lett.*, 2020, **116**, 263102.

11550 | *Phys. Chem. Chem. Phys.*, 2025, **27**, 11541–11550

This journal is © the Owner Societies 2025